

Non-contact ultrasound to assist laser additive manufacturing

Received: 30 October 2024

Accepted: 30 July 2025

Published online: 15 August 2025



Jiasen Han^{1,6}, Shuhao Wang^{2,6}, Wenjun Ge^{3,6}, Hui Chen^{1,6} , Yajing Sun¹, Yuxiang Ai¹, Weihao Yuan⁴, Siyuan Ruan⁴, Weiming Niu¹, Haiou Yang¹, Shuo Yin⁴, Wentao Yan³ & Xin Lin^{1,5} 

In ultrasound-aided laser melting processes such as additive manufacturing, it is generally believed that acoustic cavitation is essential for grain refinement during solidification while acoustic streaming plays a negligible role. We propose a non-contact ultrasound approach to provide low-intensity ultrasound, i.e., below the melt cavitation threshold, ensuring a pure acoustic streaming regime. Without cavitation, it is found that fine equiaxed grains still can be achieved. This is attributed to the combined effects of acoustic streaming and Marangoni force, which create a high-frequency-shaking type melt flow in the melt pool, leading to fatigue fracture of dendrites and thus grain refinement. Moreover, low-intensity ultrasound can offer stable melt pool modulation throughout layer-by-layer processing, enabling uniform grain refinement in large-scale samples, which is a challenge for the current direct-contact ultrasound approach.

Laser melting based additive manufacturing (AM) is currently one of the most extensively used AM techniques^{1–5}, where a high-power-intensity laser is used to melt metallic materials into a small melt pool ($\sim 10^{-4}$ – 10^{-3} m), depositing materials in a layer-by-layer manner to build 3D parts^{6–9}. The melt pool features steep temperature gradients ($\sim 10^5$ – 10^7 K·m⁻¹^{10–12}) and thus the solidification shows a strong epitaxial grain growth along the deposition direction, leading to columnar grains in the fabricated part for most metallic materials, which is detrimental for the mechanical properties^{13–16}. The ultrasound-aided melt process, a field-based method for grain refinement used in welding, cladding and casting^{17,18}, is recently employed for the laser AM process^{19,20}. Up to now, two physical mechanisms have been widely accepted for the ultrasound effect on the melt process, namely the acoustic cavitation and acoustic streaming^{19,21}. However, there is a long-standing controversy on which factor is dominant in grain refinement: acoustic cavitation, acoustic streaming flow, or the synergistic effects of both? Acoustic cavitation occurs when the ultrasonic intensity is higher than

the melt cavitation threshold, where the alternating ultrasonic pressure is believed to induce bubble formation, oscillation, growth and implosion, resulting in grain fragmentation and enhanced grain nucleation^{22,23}. Acoustic streaming, a swirling flow caused by ultrasonic vibration, is recently observed via synchrotron X-ray imaging and believed to play a role in grain refinement²⁴. Most of the existing researches claim that the acoustic cavitation is the crucial cause of grain refinement while the acoustic streaming flow has minimal impact^{25,26}, e.g., in welding²⁷, casting²⁸, and cladding and AM^{22,23,29–31}. However, the commonly used high-intensity ultrasound (more than hundreds of W·cm⁻² even with the amplitude of 2–3 μ m at the frequency of 20 kHz) is generally several orders of magnitude higher than the cavitation threshold of the melt³², and the effects of acoustic cavitation and acoustic streaming flow on the melt solidification are both active and thus difficult to be distinguished.

Another critical issue is that in all the existing research, the ultrasound is loaded into the melt pool by a contact-transmission

¹State Key Laboratory of Solidification Processing, Northwestern Polytechnical University, Xi'an, P. R. China. ²Key Laboratory of Metallurgical Equipment and Control Technology, Ministry of Education, Wuhan University of Science and Technology, Wuhan, P. R. China. ³Department of Mechanical Engineering, National University of Singapore, Singapore, Singapore. ⁴Department of Mechanical, Manufacturing and Biomedical Engineering, Trinity College Dublin, The University of Dublin, Dublin, Ireland. ⁵Key Laboratory of Metal High Performance Additive Manufacturing and Innovative Design, Ministry of Industry and Information Technology, Northwestern Polytechnical University, Xi'an, P. R. China. ⁶These authors contributed equally: Jiasen Han, Shuhao Wang, Wenjun Ge, Hui Chen. ✉ e-mail: hchen1984@nwpu.edu.cn; xlin@nwpu.edu.cn

mode to ensure the intension, i.e., the ultrasound is directly transmitted to the melt pool through the solid substrate^{19,20,25} by placing the ultrasound transducer in contact. In practical applications, the contact-transmission approach (Fig. 1b) poses a great barrier in producing uniform refined grain structures, especially when manufacturing large-size or complex-shaped parts^{19,21}. As the distance between the melt pool and ultrasonic source varies at different regions

of the part, the ultrasound transmitted into the melt pool will vary significantly with different amplitudes, and it is difficult to maintain consistent ultrasound^{19,33}. This makes the ultrasonic effects in the melt pool inconsistent and uncontrollable during the layer-by-layer AM process, resulting in inhomogeneous solidified structures and mechanical properties¹⁹, which is still an enormous challenge encountered by the current high-intensity ultrasound-aided laser AM.

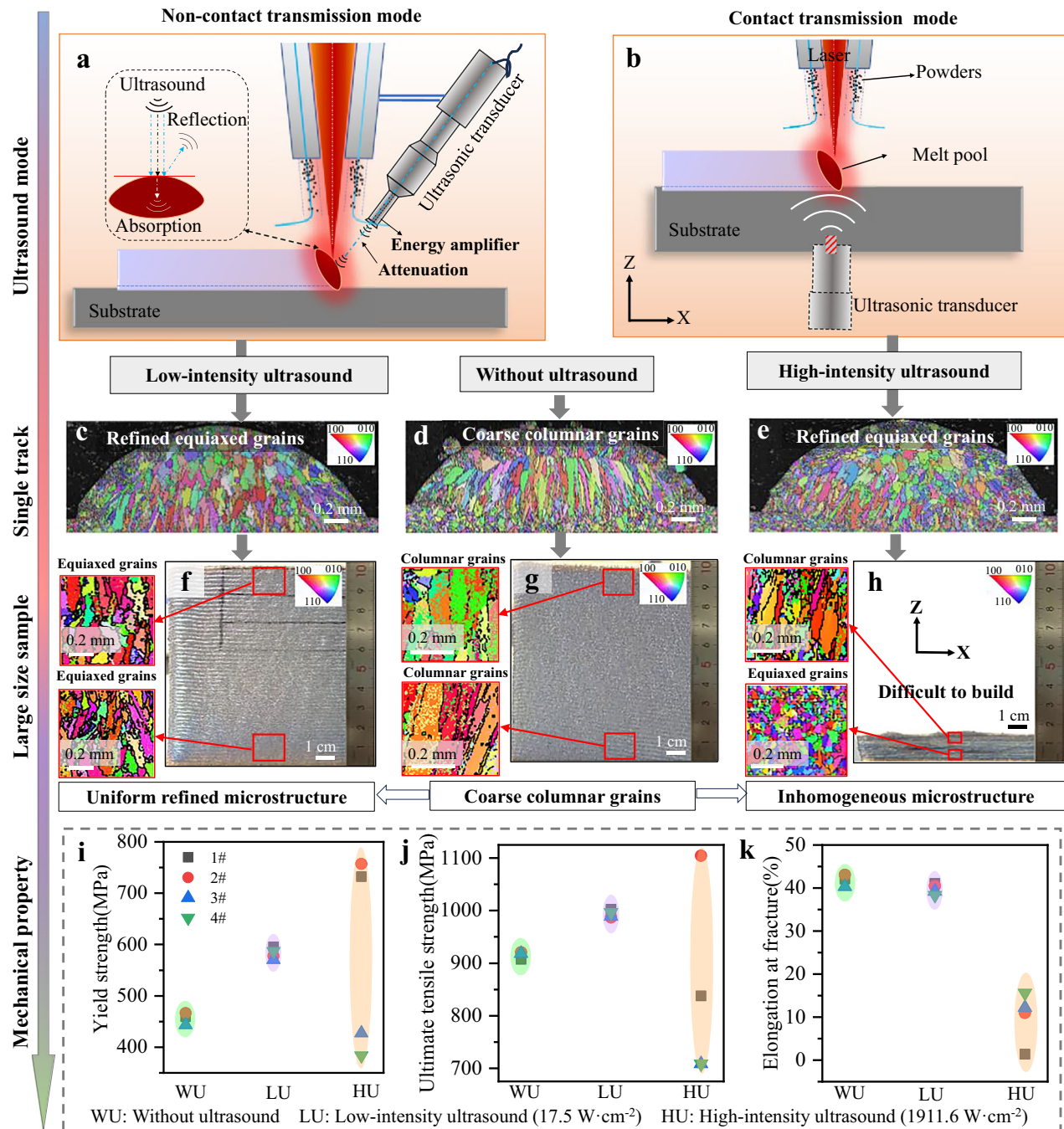


Fig. 1 | Ultrasound-aided laser melting and deposition. **a** The schematic of low-intensity ultrasound by non-contact-transmission mode. In this mode, the ultrasonic transducer with an energy amplifier is fixed with the powder feeder. The ultrasound from the transducer enters the gas medium with great attenuation and then transmits to the melt pool. Note that the energy amplifier is employed to ensure that the weakened ultrasound is still strong enough at the position of the melt pool. **b** The schematic of high-intensity ultrasound by the traditional contact-transmission mode. **c–e** Grain structure in a single track deposited with low-

intensity ultrasound (**c**), without ultrasound (**d**) and high-intensity ultrasound (**e**). **f–h** Large-size sample and microstructure with low-intensity ultrasound (**f**), without ultrasound (**g**) and high-intensity ultrasound (**h**). **i–k** Mechanical properties of as-fabricated samples, where four tensile samples are tested for each case. Inconel 718 is selected as the model material. Details of facilities and calibration of ultrasonic intensities are described in the “Methods” section and Supplementary Figs. 2 and 3. The optimized laser parameters are given in Supplementary Fig. 1 and Table 2.

In addition, as the high-intensity ultrasound causes strong bubble oscillation and shocking waves in the melt pool, it is easy to induce fusion defects such as pores and rough surfaces during the process^{20,27,34}, comprising the mechanical properties.

Here, we develop a non-contact low-intensity ultrasound-aided laser AM technique (Fig. 1a) with two objectives: 1) ensuring consistent ultrasound input to achieve uniform grain refinement and mechanical property, and 2) evaluating the effect of acoustic streaming on the laser melting process. Two common alloys, Inconel 718 and 316 L stainless steel, are employed to demonstrate the universality of conclusions. Surprisingly, the non-contact low-intensity ultrasound approach is able to induce refined grains, and more importantly, ensure uniform refined structures with less fusion defects in the layer-by-layer AM process of large-size samples, overcoming the critical barrier of the current approach. Leveraging systematic experimental characterizations and high-fidelity modeling, the physical mechanisms of grain refinement by non-contact low-intensity ultrasound, such as columnar-to-equiaxed-transition (CET), plastic fracture and fatigue fracture of dendrites, are investigated quantitatively. The results profoundly enhance the fundamental understanding of the ultrasound-aided laser melting process, and our non-contact low-intensity ultrasound approach is a promising solution to control microstructure and mechanical properties in melting-based AM and many other techniques, such as cladding and welding.

Results

Superiority of non-contact low-intensity ultrasound

The non-contact ultrasound approach (Fig. 1a) is designed to provide consistent low-intensity ultrasound below the melt cavitation threshold in the melt pool, where the ultrasound transducer maintains a constant distance with the melt pool by moving together with the nozzle (more details in Methods and Supplementary Fig. 2b). For comparison, the laser AM experiments without ultrasound and with conventional contact-transmission high-intensity ultrasound (Fig. 1b) are also conducted. Contact-transmission ultrasound can indeed remarkably refine the solidified structures in single track experiments with the model materials, where the coarse columnar grains (Fig. 1d) are totally refined to equiaxed grains (Fig. 1e). However, in the multi-layer AM process of a large-size sample, the contact-transmission high-intensity ultrasound mode fails to consistently refine grain structures, due to the significant transmission loss of ultrasonic energy with the increasing distance from the ultrasound source, where the grain size varies with position in the sample and columnar grains appear above a certain height (~10 mm in Fig. 1h). Actually, as the high-intensity ultrasound leads to fusion defects, it is difficult to build a block sample higher than 15 mm (Fig. 1h).

Surprisingly, the low-intensity ultrasound, only with the acoustic streaming effect, can also induce refined grain structures (Fig. 1c), which corrects the traditional cognition that ultrasound without cavitation is negligible for grain refinement. More importantly, as consistent and controllable ultrasound can be provided in the melt pool by moving the ultrasonic source and nozzle together during the layer-by-layer AM process, uniformly refined grain structures with little fusion defects are obtained throughout the large-size sample with the height of ~100 mm (Fig. 1f). That is, our non-contact low-intensity ultrasound approach retains the positive effect of grain refinement, and eliminate the detrimental effect of fusion defects, thereby perfectly overcoming the challenges encountered by the conventional contact-transmission ultrasound mode.

Consequently, the mechanical properties of parts by the non-contact low-intensity ultrasound-aided laser AM are remarkably enhanced. Compared with that without ultrasound, the yield stress and ultimate tensile strength of Inconel 718 are enhanced by ~27.6 % (from 456 to 582 MPa) (Fig. 1i) and 8.6 % (from 915 to 994 MPa) (Fig. 1j), with negligible reduction of plasticity (from 41.5 to 40.1 %) (Fig. 1k).

More significantly, the quality consistency is obviously enhanced, where the values of tensile properties are highly repeatable with little variation. This is attributed to the uniform refined microstructure under the consistent and controllable ultrasonic effect. In contrast, the mechanical properties by the high-intensity ultrasound show a large variation (Fig. 1i–k), which is attributed to the fusion defects and inhomogeneous microstructure due to the inconsistent ultrasonic effect. For instance, the yield strength of tensile samples by the high-intensity ultrasound varies in a big range from 427 to 757 MPa (Fig. 1i), showing poor quality consistency. This means the low-intensity ultrasound by our non-contact-transmission mode has the advantage in reproducibility, which is critical for laser AM. In addition to laser AM, the grain refinement mechanism of our non-contact low-intensity ultrasound approach is expected to be universal in such melting processes and has promising applications in other techniques such as laser cladding and welding.

Fusion defects

Similar to some previous reports³⁵, our detailed results confirm that the high-intensity ultrasound leads to fusion defects such as bulges, pits, coarse ripples and even discontinuity in the melted single tracks, and the stronger the ultrasonic intensity is, the more serious the fusion defects are (Fig. 2f, g, i). In contrast, with the low-intensity ultrasound, no obvious fusion defects are discovered (Fig. 2b–e, h), and the smooth and continuous single tracks are comparable to that without ultrasound (Fig. 2a). The shape of single track is further investigated in terms of the aspect ratio (Fig. 2j), where the width and height of the track cross section are detailed in Supplementary Fig. 4. The aspect ratio of the melted track increases with the increase of the ultrasonic intensity, i.e., the track becomes wider and flatter. However, the increment of aspect ratio by the low-intensity ultrasound (from 2.91 to 3.23) is negligible, compared with the remarkable increment by high-intensity ultrasound (from 2.91 to 6.9). Considering the fusion defects caused by high-intensity ultrasound, such a tendency by high-intensity ultrasound will make it difficult to accomplish the layer-by-layer deposition of block parts. Under the ultrasound intensity of 2855.6 W·cm⁻², the single track becomes discontinuous and collapsed (Fig. 2i), and hence, the multilayer melting and deposition of a block sample cannot be accomplished successfully. Pore defects in the deposited block samples are tested by X-ray computed tomography. It is found that the stronger ultrasound results in more pores within the block samples (Fig. 2k–o). Quantitative plots indicate that the increase of porosity caused by the low-intensity ultrasound (from 7.9 to 17.5 W·cm⁻²) is ignorable compared with that caused by the high-intensity ultrasound (from 212.4 to 1911.6 W·cm⁻²) (Fig. 2p). With low-intensity ultrasound, the samples are deposited with near full density, which is comparable to that without ultrasound. These confirm that the non-contact low-intensity ultrasound effectively avoids fusion defects, which are remarkable under the high-intensity ultrasound. Similar conclusions can be drawn from the results of 316 L stainless steel (Supplementary Fig. 5).

Grain structures

The major objective of using ultrasound in laser melting is to tailor the grain structures, mainly achieving grain refinement. Figure 3 depicts the effects of ultrasound on the crystal structure of Inconel 718 single tracks. The sample without ultrasound is featured by columnar grains with several millimeters in length (Fig. 3a, g), which is a typical grain structure caused by the steep temperature gradient. As expected, the high-intensity ultrasound shows a strong ability of grain refinement, inducing fully refined equiaxed grains with random orientations (Fig. 3e, f, i). Surprisingly, the non-contact low-intensity ultrasound can lead to refined grain structure with the intensities of 14 W·cm⁻² and 17.5 W·cm⁻² (Fig. 3c, d, h), while the grain refinement is not so pronounced when the intensity is smaller than 10.5 W·cm⁻² (Fig. 3b).

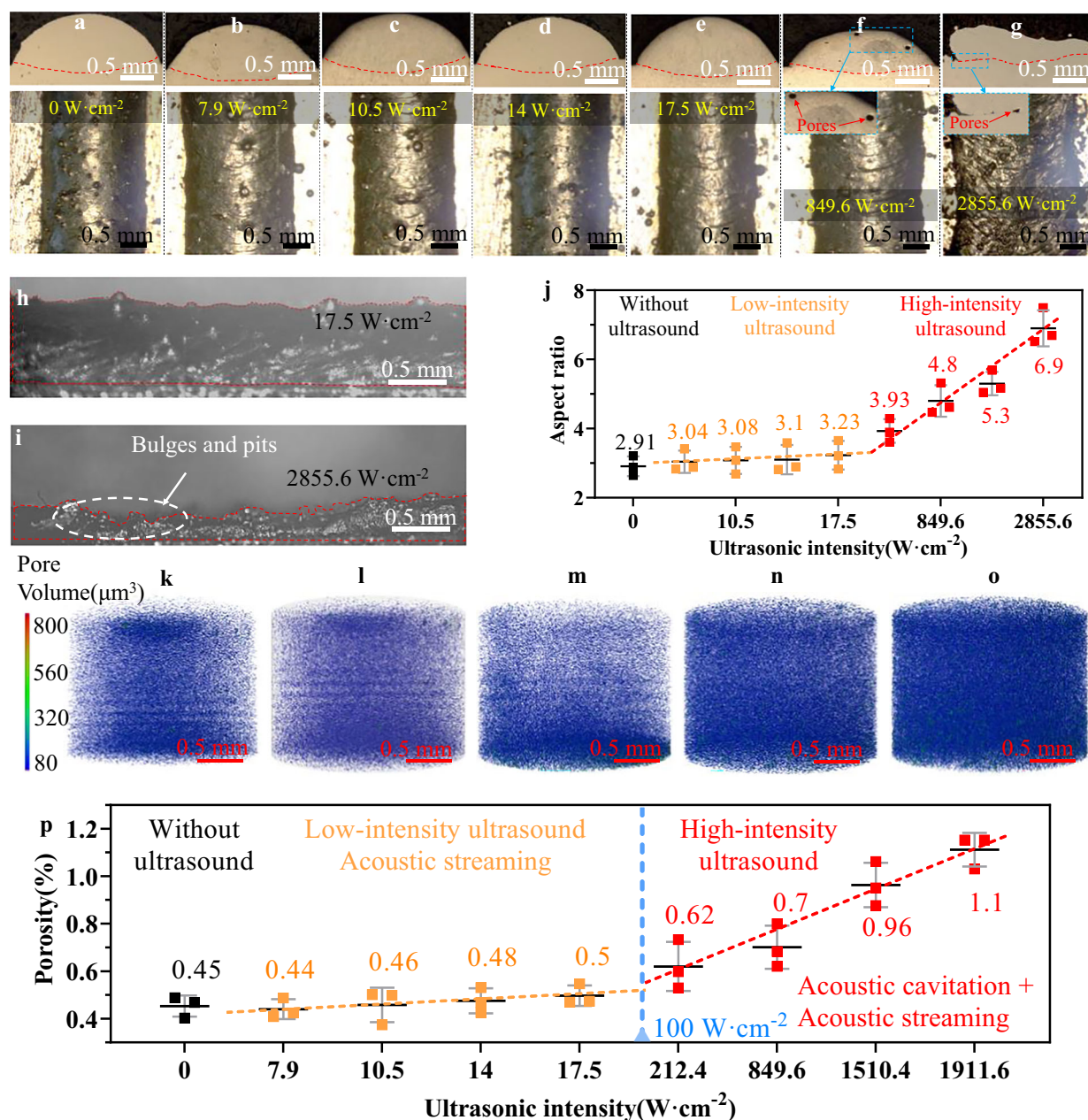


Fig. 2 | Effect of ultrasound on fusion defects of Inconel 718. **a–g** Single tracks melted without ultrasound (**a**), with low-intensity (**b–e**) and high-intensity ultrasound (**f, g**). The red dashed lines indicate the fusion boundaries. **h, i** The lateral morphology of single track with the ultrasonic intensity of $17.5 \text{ W}\cdot\text{cm}^{-2}$ and $2855.6 \text{ W}\cdot\text{cm}^{-2}$. **j** The aspect ratio (the ratio of width to height) of single tracks with different ultrasonic intensities. **k–o** X-ray computed tomography showing the

pore defects of block samples with the ultrasonic intensities of $0 \text{ W}\cdot\text{cm}^{-2}$ (**k**), $10.5 \text{ W}\cdot\text{cm}^{-2}$ (**l**), $17.5 \text{ W}\cdot\text{cm}^{-2}$ (**m**), $849.6 \text{ W}\cdot\text{cm}^{-2}$ (**n**) and $1911.6 \text{ W}\cdot\text{cm}^{-2}$ (**o**). **p** The variation of porosity with the ultrasonic intensity from 0 to $1911.6 \text{ W}\cdot\text{cm}^{-2}$. The results of 316 L stainless steel are attached in Supplementary Fig. 5. The length of error bars in Fig. 2 j, p indicates the dispersion of data in three tests.

Figure 3j quantifies the correlation between the grain size and ultrasonic intensity for the single tracks. Compared with the average grain size of $73.7 \mu\text{m}$ without ultrasound, the grain refinement by high-intensity ultrasound is obvious, reducing the average grain size to $30.2 \mu\text{m}$ under the ultrasonic intensity of $849.6 \text{ W}\cdot\text{cm}^{-2}$, and the grain refinement by low-intensity ultrasound is not so remarkable until it reaches to $17.5 \text{ W}\cdot\text{cm}^{-2}$. By the low-intensity ultrasound of $17.5 \text{ W}\cdot\text{cm}^{-2}$, the refined grain size ($44.6 \mu\text{m}$) is even comparable to the high-intensity ultrasound of $212.4 \text{ W}\cdot\text{cm}^{-2}$.

In previous ultrasound-aided melt processes, it is commonly believed that acoustic cavitation is essential for producing a great number of crystal nucleus and thus grain refinement, while the acoustic streaming is just responsible for the grain transporting and

distributions³⁶. Considering the small size of the melt pool in the condition of laser melting, the effect of acoustic streaming on the grain refinement is even deemed to be negligible, as the entire melt pool is completely covered by the cavitation¹⁹. However, our results identify that the fine equiaxed grains can also be produced by the low-intensity ultrasound below the melt cavitation threshold, showing the ability of low-intensity ultrasound with pure acoustic streaming in the grain refinement, which corrects the long-standing inaccurate intuition.

To further assess the effect of ultrasound in layer-by-layer deposition process, block specimens are deposited (Fig. 4a–j) by a single-track-deposition strategy (Supplementary Fig. 1). As expected, the sample without ultrasound is featured by the typical epitaxially grown crystal structure, where columnar grains with an average size of

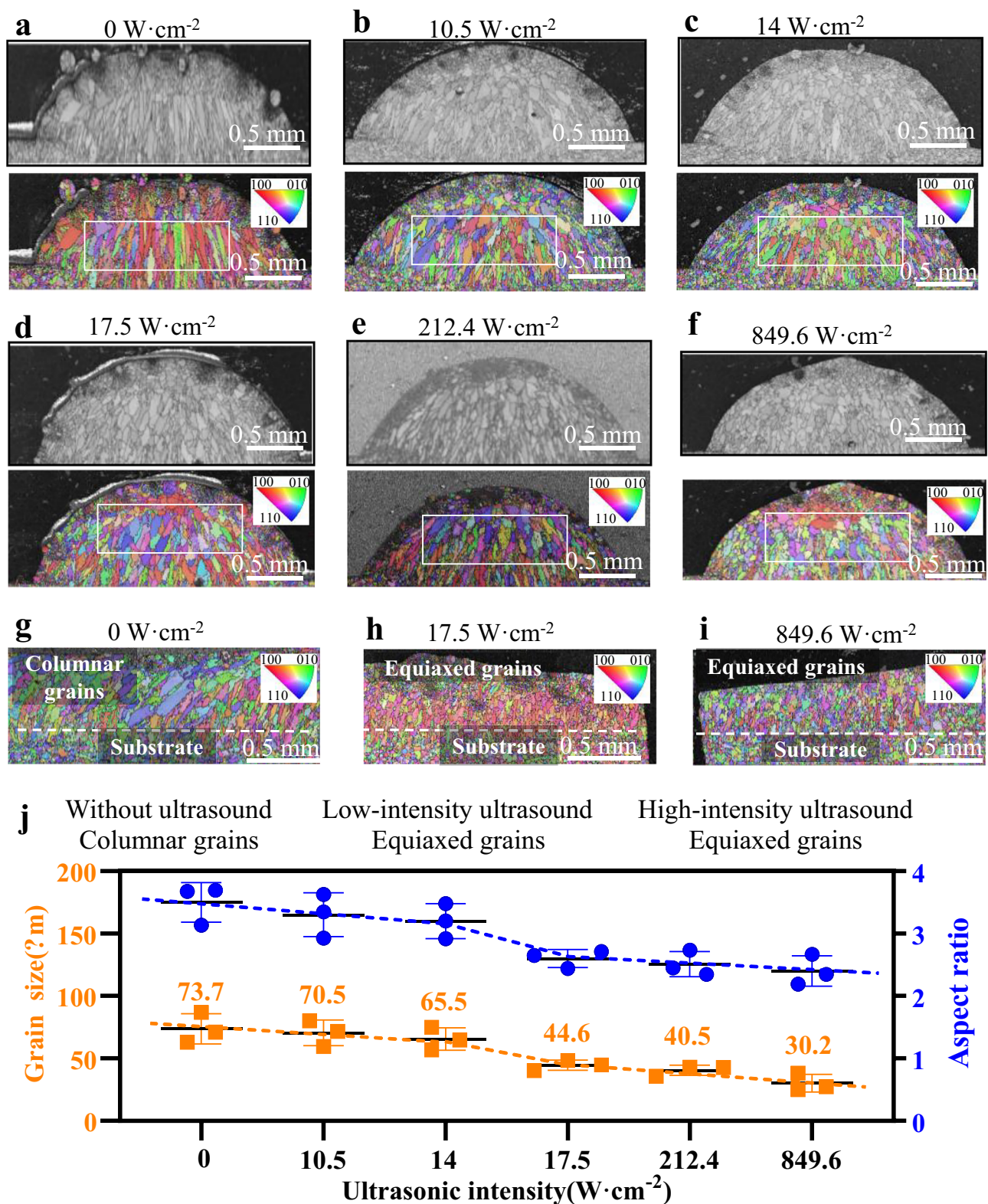


Fig. 3 | Effect of ultrasound on grain structure of Inconel 718 single tracks. **a–f** Cross-section inverse pole figure (IPF) plots of single tracks without ultrasound (**a**), with low-intensity ultrasound of $10.5 \text{ W}\cdot\text{cm}^{-2}$ (**b**), $14 \text{ W}\cdot\text{cm}^{-2}$ (**c**) and $17.5 \text{ W}\cdot\text{cm}^{-2}$ (**d**), and with high-intensity ultrasound of $212.4 \text{ W}\cdot\text{cm}^{-2}$ (**e**) and $849.6 \text{ W}\cdot\text{cm}^{-2}$ (**f**). **g–i** Lateral IPF plots of single tracks (profile along scanning direction of the single fusion track) with the ultrasonic intensity of $0 \text{ W}\cdot\text{cm}^{-2}$ (**g**), $17.5 \text{ W}\cdot\text{cm}^{-2}$ (**h**) and $849.6 \text{ W}\cdot\text{cm}^{-2}$ (**i**). **j** Variations of grain size and aspect ratio (the ratio of grain length

to width) of the single tracks with the ultrasonic intensity from 0 to $849.6 \text{ W}\cdot\text{cm}^{-2}$. To avoid the influence of the unique thermal environment on the top of the fused track and substrate on grain growth, the analysis of the grain size and aspect ratio is limited in the central region of the sample (the region selected by the white box in Fig. 3a–f). Details of the grain size distribution of Inconel 718 single tracks can be found in Supplementary Fig. 6. The length of error bars in Fig. 3j indicates the dispersion of data in three tests.

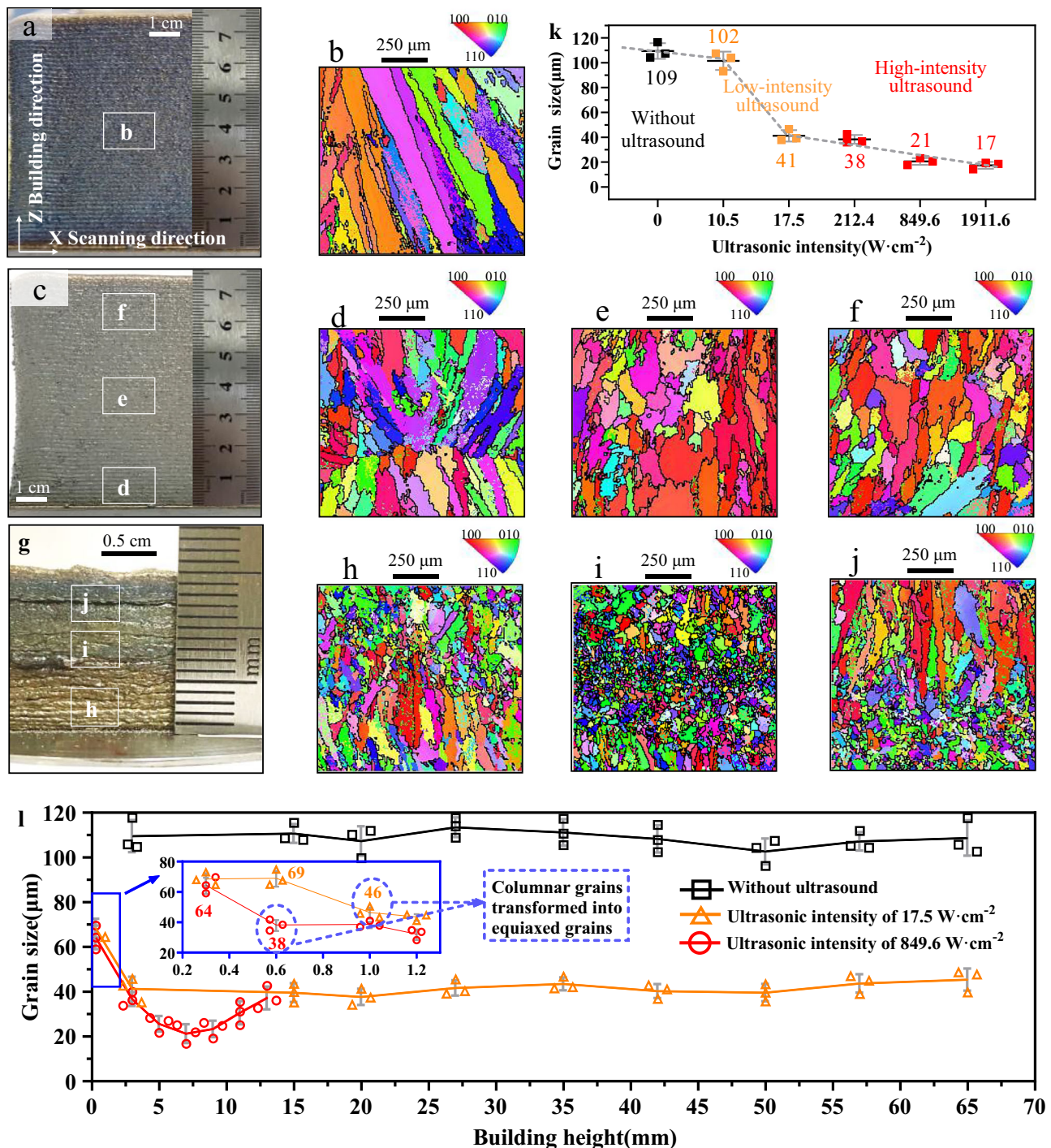


Fig. 4 | Effect of ultrasound on grain structure of Inconel 718 block samples. **a–g** Specimens deposited without ultrasound (**a**), with low-intensity ultrasound of $17.5 \text{ W}\cdot\text{cm}^{-2}$ (**c**), and high-intensity ultrasound of $849.6 \text{ W}\cdot\text{cm}^{-2}$ (**g**). The corresponding grain structures are characterized along the building direction (vertical direction). **b** IPF plot of specimen by ultrasonic intensity of $0 \text{ W}\cdot\text{cm}^{-2}$. **d–f** IPF plots at different positions of the specimen by ultrasonic intensity of $17.5 \text{ W}\cdot\text{cm}^{-2}$; bottom zone (**d**), middle zone (**e**), and top zone (**f**). **h–j** IPF plots at different positions of the

specimen with ultrasonic intensity of $849.6 \text{ W}\cdot\text{cm}^{-2}$; bottom zone (**h**), middle zone (**i**), and top zone (**j**). **k** Grain size in equiaxed grain zone of block samples by different ultrasonic intensities. **l** Grain size along the building height of block samples. Details of grain size and inverse pole maps can be found in Supplementary Fig. 9. Results of 316 L stainless steel are attached in Supplementary Fig. 8. The length of error bars in Fig. 4k, l indicates the dispersion of data in three tests.

$109 \mu\text{m}$ parallel grown along the building direction (Fig. 4b). When the ultrasound is loaded, however, the first few layers (about 2–3 layers) exhibit refined columnar grains along the building direction for both the non-contact low-intensity ultrasound (Fig. 4d) and contact high-intensity ultrasound (Fig. 4h), rather than refined equiaxed grains in the conditions of single tracks (Fig. 3d, f). This can be attributed to the

steep temperature gradient from the cold substrate to the first few layers, where the epitaxial grain growth during the interlayer remelting overcomes the effects of grain refinement of the ultrasound. As the building height increases, the interlayer temperature gradient decreases due to the heat accumulation, and then the ultrasonic effects dominate the fusion process, and hence the samples turn to

refined equiaxed grain structures (Fig. 4e, i). Since the high-intensity ultrasound of $849.6 \text{ W}\cdot\text{cm}^{-2}$ has a stronger effect than the low-intensity ultrasound of $17.5 \text{ W}\cdot\text{cm}^{-2}$, its conversion position of equiaxed grain structure ($Z \approx 0.6 \text{ mm}$) is lower than that of the low-intensity ultrasound of $17.5 \text{ W}\cdot\text{cm}^{-2}$ ($Z \approx 1.0 \text{ mm}$) (enlarged view in Fig. 4l). In the equiaxed grain zone of block samples, the grain refinement of low-intensity ultrasound of $17.5 \text{ W}\cdot\text{cm}^{-2}$ can be comparable to the high-intensity ultrasound of $212.4 \text{ W}\cdot\text{cm}^{-2}$ (Fig. 4k), which is similar to the condition of single tracks.

Importantly, in the non-contact-transmission ultrasound mode (Fig. 1a), as the ultrasound transducer is fixed with the nozzle and maintains a constant distance with the melt pool, the ultrasonic energy in the melt pool is stable and consistent, regardless of the size and geometry of the sample. Therefore, when the building height keeps increasing, the non-contact low-intensity ultrasound is always effective and creates a uniform refined grain structure throughout the sample (Fig. 4e, f, l). However, for the contact-transmission high-intensity ultrasound, the refined equiaxed grains gradually become coarser along the building direction and turn back into column grains again at the building height of $Z \approx 10 \text{ mm}$ (Fig. 4j, l), indicating that the ultrasonic effect is weakened at this position. Unlike our non-contact ultrasound mode, the distance between the ultrasound source and melt pool in the contact-transmission mode is instantaneously changing, and then the intensity of ultrasound in the melt pool is not stable during the process, especially along the building height featuring a periodic intensity¹⁹. We measured the ultrasonic amplitude along the building height of the sample (Supplementary Fig. 7). The ultrasonic vibration attenuates gradually along the building height and almost disappears at the height of 15 mm (about half of the fading period in our condition). This shows that the effect of contact-transmission high-intensity ultrasound is not stable in the layer-by-layer process. A similar phenomenon is also identified in the 316 L stainless steel sample (Supplementary Fig. 8).

Owing to the inhomogeneous microstructures produced by the contact-transmission high-intensity ultrasound, the values of mechanical properties of samples show poor consistency, although some high values of strength can be obtained (Fig. 1i–k). In contrast, the mechanical properties of samples produced by non-contact-transmission low-intensity ultrasound are highly repeated with little variation (Fig. 1i–k), which is attributed to the uniform refined microstructures and less fusion defects.

The results show the superiority of low-intensity ultrasound by our non-contact-transmission mode in producing large-size part with uniform refined microstructures. Theoretically speaking, the great challenge of producing constant energy in melt pool by traditional contact-transmission approach¹⁹ can be solved by accurate and real-time regulation on the output of the ultrasound and then uniform microstructures can be made in large-size part. However, we believe that the non-contact ultrasound approach provides another convenient and applicable way.

Discussion

The key physical phenomena in this work are that the low-intensity ultrasound below the melt cavitation threshold is also able to refine grain structures, and meanwhile induces fewer fusion defects than the high-intensity ultrasound. The underlying mechanisms are explored by leveraging in-situ monitoring, post-process characterizations and high-fidelity multi-physics simulations.

As revealed by the in-situ monitoring and corresponding simulations, the morphology of the melt pool under low-intensity ultrasound (Fig. 5b, e and the Supplementary Movies 2 and 5) is quite similar to that without ultrasound (Fig. 5a, d and the Supplementary Movies 1 and 4), showing a convex and relative stable surface with gas-induced mild fluctuations during the deposition process. The melt pool flow by high-intensity ultrasound is much fiercer, showing a

depressed surface with shaking fish-scale ripples (Fig. 5c, f and the Supplementary Movies 3 and 6), which is also reported previously^{20,34}. Without ultrasound, the typical steady vortex flow dominated by Marangoni force³⁷ is clear in the cross section of the melt pool (Fig. 5g and Supplementary Movie 7). The non-contact low-intensity ultrasound induces acoustic pressure on the melt pool surface, which, together with the Marangoni force, leads to a high-frequency-shaking pattern flow within the melt pool (Fig. 5h and Supplementary Movie 8). As the ultrasonic effect is not strong enough, the overall flow pattern of the melt pool remains similar and steady, with a slight forward and upward movement. Consequently, the stable melt pool ensures the excellent surface quality of the fused track. Under high-intensity ultrasound (Fig. 5i and Supplementary Movie 9), however, the powerful ultrasonic vibration dominates over the Marangoni flow. Specifically, when the vibration-induced strong inertial force acts towards the negative Z-axis, the melt flows downward and forward with high speed, generating a concave surface with ripples. The upward inertial force elongates the melt pool rear and creates an unstable tail region, leading to the fusion defects such as discontinuities, large bumps, and depressions.

Compared with acoustic cavitation, the grain refinement mechanisms of low-intensity ultrasound with acoustic streaming are obviously different and have never been explored, which will be discussed below. Significantly, this work is not claiming that one mechanism overpasses the other. As the strong effect of acoustic cavitation by high-intensity ultrasound on the grain refinement is commonly recognized, it will not be discussed here.

Compared with the case without ultrasound, one difference made by the low-intensity ultrasound is the varied flow pattern in the melt pool, which inevitably influences the temperature distribution of the melt pool, especially in the mushy zone. The varied temperature gradient (G) and solidification rate (R) may prompt the columnar-to-equiaxed-transition (CET) during solidification. In this regard, the corresponding G and R values are extracted and evaluated using the extended Hunt criterion^{38–40}. The G^2R^{-1} value in the solidification front is always higher than the columnar threshold, even when the low-intensity ultrasound is loaded (detailed in Supplementary Fig. 12 and Supplementary Movies 10 and 11). This indicates that the CET cannot happen and is not responsible for the grain refinement under low-intensity ultrasound.

The plastic fracture of dendrites caused by the impact of melt flow in the mushy zone is another possible reason for grain refinement. The dynamical features of dendrites in melt flow can be described as²⁰:

$$\sigma_f = \frac{6\mu v L^2}{r^3} \quad (1)$$

where σ_f is the stress in the dendrite caused by the melt flow, $\mu = 0.006 \text{ kg}\cdot(\text{m}\cdot\text{s})^{-1}$ ²⁰ is the viscosity, v is the melt flow speed, L is the dendrite arm length, and r is the radius of the secondary dendrite arm. By the morphology of the microstructure (Supplementary Fig. 10), a dendrite arm with size $L = 60 \mu\text{m}$ and $r = 1.45 \mu\text{m}$ is selected as an example. The melt flow speed v in the mushy zone without ultrasound and with low-intensity ultrasound can reach the maximum of $0.726 \text{ m}\cdot\text{s}^{-1}$ (Fig. 5j and Supplementary Movie 12) and $1.678 \text{ m}\cdot\text{s}^{-1}$ (Fig. 5k and Supplementary Movie 13), and thus induces the maximum stress σ_f of 30.9 MPa and 71.3 MPa according to Eq. (1), respectively. As the yield strength of Inconel 718 dendrites at the temperature of 1609.15 K is 37.3 MPa ^{20,41} (Supplementary information: C. Dendrite stress and fatigue fracture behavior - 2) Yield stress of dendrite), it can be concluded that the melt flow without ultrasound cannot break the dendrite arms, while the addition of low-intensity ultrasound will cause more significant plastic deformation of dendrites. However, as the fracture strength of Inconel 718 dendrites in the mushy zone is currently not available⁴¹, strictly speaking, it is unable to judge whether

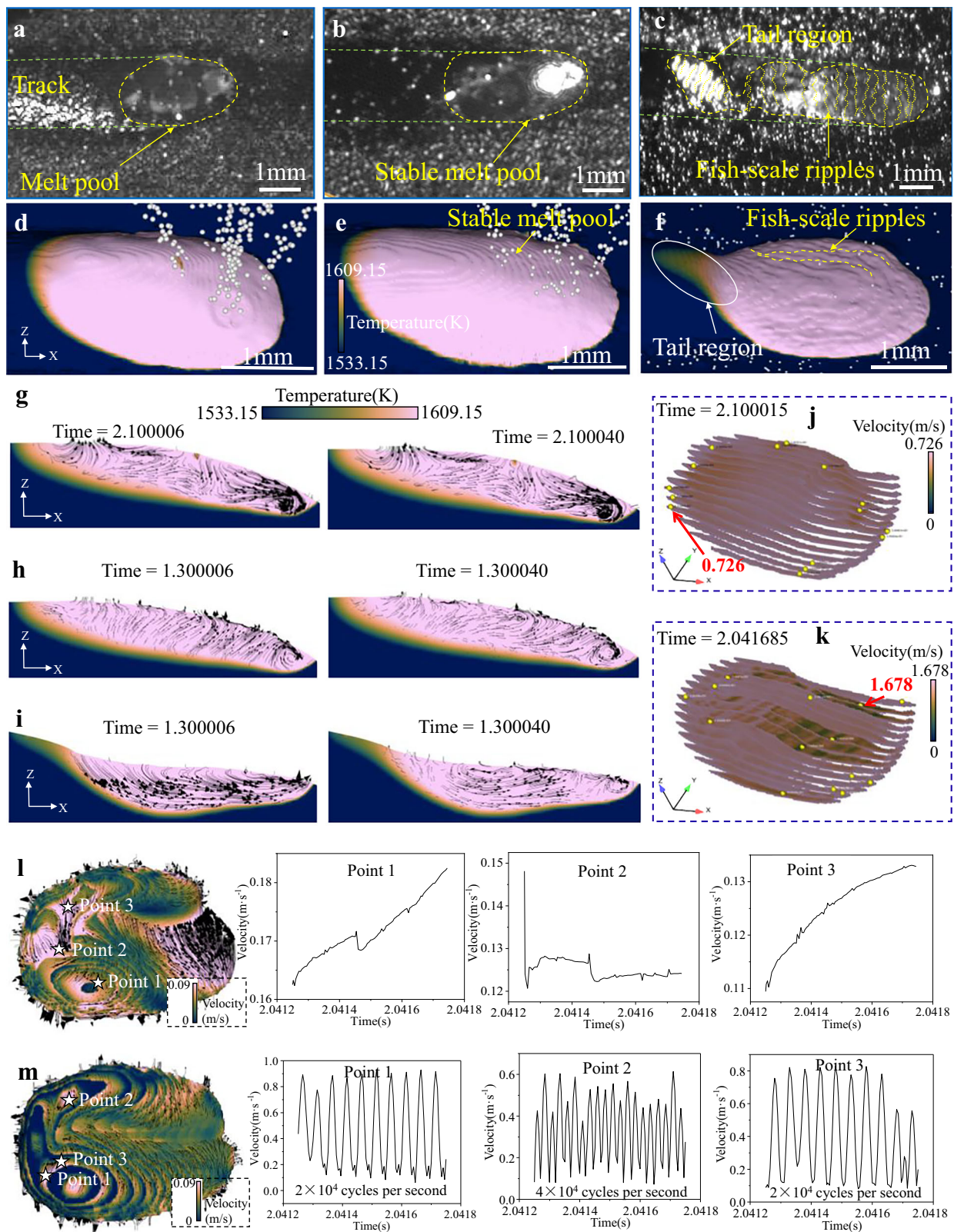


Fig. 5 Melt pool evolution with ultrasound. **a–c** High-speed camera images of melt pool surface morphologies under the ultrasonic intensity of 0 W·cm⁻² (**a**), 17.5 W·cm⁻² (**b**) and 849.6 W·cm⁻² (**c**), respectively. **d–f** Simulation results showing the melt pool surface morphologies under the ultrasonic intensity of 0 W·cm⁻² (**d**), 17.5 W·cm⁻² (**e**) and 849.6 W·cm⁻² (**f**), respectively. **g–i** Velocity profiles in the cross section of the melt pool under the ultrasonic intensity of 0 W·cm⁻² (**g**), 17.5 W·cm⁻² (**h**) and 849.6 W·cm⁻² (**i**). **j, k** The maximum transient flow velocity in the mushy

zone of the melt pool under the ultrasonic intensity of 0 W·cm⁻² (**j**) and 17.5 W·cm⁻² (**k**). **l, m** Variation of flow velocity with time at three points in the mushy zone of the melt pool with the ultrasonic intensity of 0 W·cm⁻² (**l**) and 17.5 W·cm⁻² (**m**). The velocity illustrated in the figure corresponds to the resultant velocity of X, Y, and Z components. The Supplementary Movies 1–15 are attached in the Supplementary file.

the melt flow under low-intensity ultrasound can cause the plastic fracture of dendrites or not.

As mentioned above, the melt pool flow driven by the low-intensity ultrasound and Marangoni force is a high-frequency-shaking type acoustic streaming flow (Supplementary Movie 8), rather than the steady-centrifugal-convection type acoustic streaming flow observed in bulk melt conditions³⁷. Without ultrasound, the flow velocity in the mushy zone gradually increases or decreases in a certain direction (points in Fig. 5l and Supplementary Movie 14). However, when the low-intensity ultrasound is added, the flow velocity is featured by high frequency fluctuating at different positions of the mushy zone (points in Fig. 5m and Supplementary Movie 15), leading to high frequency cyclic drag forces on the dendrite arms and hence possible fatigue fracture. The fatigue life of the dendrites in the mushy zone can be estimated by the Basquin equation⁴²:

$$S_a = S'_f (2N_f)^b \quad (2)$$

where N_f is the fatigue life, S_a is the fatigue strength amplitude, $S'_f = 2.8 \sigma_y$ is the fatigue strength coefficient ($\sigma_y = 37.3 \text{ MPa}$ ^{20,41} is the yield strength), and $b = -0.26$ is the fatigue strength index (The determination of S'_f and b is detailed in Supplementary information: C. Dendrite stress and fatigue fracture behavior). For the low-intensity ultrasound case, we randomly selected several regions within the mushy zone and extracted the temporal evolution of their velocities, as shown in Fig. 5m. Both Point 1 and Point 3 exhibited a velocity frequency of 20 kHz, with average velocity amplitudes of approximately $0.41 \text{ m}\cdot\text{s}^{-1}$ and $0.33 \text{ m}\cdot\text{s}^{-1}$, respectively. Taking the dendrite arm above, for example, the stress in the dendrite arm caused by the melt flow σ_f is calculated as 17.4 MPa and 14 MPa by Eq. (1), respectively, i.e., the S_a is respectively 17.4 MPa and 14 MPa for the two points. Thus, it can be evaluated by Eq. (2) that the fatigue life of dendrites N_f is lower than 488 cycles (Point 1 in Fig. 5m) and 1134 cycles (Point 3 in Fig. 5m). In low-intensity ultrasound case, the maximum surviving time of the mushy zone is approximately 0.134 seconds (detailed in Supplementary Fig. 13). The periodical impact of melt flow on the dendrites is about 2680 cycles during the 0.134 seconds under the effect of 20 kHz ultrasonic vibration, meaning that the fatigue fractures of dendrites (Point 1 & 3 in Fig. 5m) can occur.

Furthermore, we conduct a series of fatigue fracture analyses on dendrite arms with different geometries (Supplementary information: C. Dendrite stress and fatigue fracture behavior - 5). Evaluation on fatigue behaviors of other dendrite arms). The findings reveal that dendrite arms with longer length or smaller diameter are more susceptible to fatigue fracture, while some of the shorter and thicker dendrite arms are less likely to experience fatigue-induced failure. It should be mentioned that the dendrite arms (Supplementary Fig. 10) are selected from the solidified structure, where the dendrites are fully grown already. In practice, when the dendrites grow from small to large gradually, they are continuously subjected to ultrasonic impacts, which may result in fatigue fragmentation easier before they have fully grown. Another interesting thing is that some ultra-high frequency melt flow (nearly 40 kHz) is found in the mushy zone (Point 2 in Fig. 5m), indicating a higher potential for melt-flow-induced fatigue fracture of dendrites. The ultra-high frequency melt flow in the melt pool may result from the phase discrepancies of the periodic inertial forces by the ultrasound, which will not be discussed further in this work.

In addition to laser AM, the non-contact-transmission low-intensity ultrasound mode can be conveniently adapted and applied for other laser melting conditions such as laser cladding and welding, and the physical mechanisms of grain refinement by low-intensity ultrasound is expected to be universal. Nevertheless, the quantitative effects of ultrasound would change to some extent, as the melt pool

behaviors, such as melt pool size, shape, and strength of Marangoni flow, are quantitatively different in other conditions.

In summary, we reveal that the non-contact low-intensity ultrasound with pure acoustic streaming has the ability to induce uniform and refined grain structures in laser AM of large and complex-shaped parts, although the grain refinement is not so remarkable as the high-intensity ultrasound. It corrects the long-standing inaccurate speculation that the acoustic streaming is a negligible factor, and provides a new understanding that the combined action of acoustic streaming and Marangoni force generates a high-frequency-shaking type melt pool flow, leading to fatigue fracture of dendrites in the mushy zone and thus the grain refinement. Moreover, by the non-contact low-intensity ultrasound technique, it is convenient to provide stable and consistent ultrasonic effects in the melt pool to ensure homogeneous refined grain structures for large complex-shaped parts, which is a challenge for the contact-transmission high-intensity ultrasound approach. The conclusions are generally applicable to metallic materials such as Inconel 718 and stainless steel 316 L. This non-contact low-intensity ultrasound technique can be extended to a broad range of conditions such as laser AM, cladding, welding and polishing, where the moving melt pool is tiny and with inherent strong melt flow.

Methods

Low-intensity versus high-intensity ultrasound

Nickel-based alloy Inconel 718 powder is selected as the model material. Furthermore, 316 L stainless steel powder is used for additional experiments to demonstrate the generality of the conclusion. The ultrasonic intensity in the melt pool (I_m) is described as ref. 19 $I_m = 0.5 \rho_m c_m (2\pi f_m A_m)^2$, where ρ_m is the material density, and c_m , f_m , and A_m are the speed, frequency and amplitude of the ultrasound in the material, respectively. With the commonly used contact-transmission mode to introduce ultrasound (Fig. 1b), the ultrasound is transmitted through the substrate into the melt pool, where the substrate material is the same as the feeding powder of the melt pool. Given the little variation of density and sound speed between the substrate (solid state) and the melt pool (liquid state), the ultrasound dissipation at the solid-liquid interface is negligible¹⁹. The ultrasound amplitude on the substrate surface can be measured (Supplementary Fig. 2a and 3a) and considered as that in the melt pool A_m , which is used to calculate the ultrasonic intensity in the melt pool (I_m). The amplitude of ultrasound at 20 kHz on the substrate surface provided by our equipment ranges from 3 to 15 μm . Note that 3 μm is the minimum amplitude that can be stably provided. For the Inconel 718 with a density of $7400 \text{ kg}\cdot\text{m}^{-3}$ and sound speed of $4047 \text{ m}\cdot\text{s}^{-1}$ ⁴³, the minimum ultrasonic intensity with the amplitude of 3 μm is calculated as $212.8 \text{ W}\cdot\text{cm}^{-2}$, which is above the cavitation threshold of melt ($100 \text{ W}\cdot\text{cm}^{-2}$ ^{19,20}). Likewise, the minimum ultrasonic intensity is also greater than the cavitation threshold of stainless steel 316 L melt. In the literatures studying other metals, it can be estimated that the employed ultrasound with an amplitude of several tens of microns is much higher than the melt cavitation threshold¹⁹. It means that both the acoustic cavitation and acoustic streaming exist in the melt pool, which is defined as the condition of high-intensity ultrasound (or cavitational ultrasound).

As mentioned above, the employed ultrasonic intensity provided by the contact-transmission mode is always higher than the cavitation threshold of the melt, even with the minimum amplitude of 3 μm . Then, we design a non-contact-transmission mode to provide ultrasound below the melt cavitation threshold (Fig. 1a). As the density and sound speed of the gas medium are much smaller than the solid transducer, the ultrasound from the transducer will be significantly weakened when entering the gas medium and propagating to the melt pool. In addition, the ultrasonic energy will further dissipate and become weaker when transmitting from the gas into the melt pool. We develop a non-invasive testing approach by a high-precision laser

displacement sensor to measure the ultrasonic amplitude (A_m) of the melt pool surface and then calculate the ultrasound energy absorbed by the melt pool (I_m) accurately. The measurement on the ultrasonic intensity in the gas (I_g) and in the melt pool (I_m) for the non-contact ultrasound is detailed in Supplementary Figs. 2b and 3b–d. By adjusting the output power of the ultrasonic device, different ultrasonic intensities within the melt pool can be achieved. Considering the high energy dissipation of the non-contact ultrasound, an energy amplifier (Fig. 1a and Supplementary Fig. 2b) is employed to ensure the weakened ultrasound is still effective in the melt pool. By our non-contact-transmission equipment, the amplitude of ultrasound in the gas medium A_g (Argon with density of $1.784\text{ kg}\cdot\text{m}^{-3}$ and sound speed of $331\text{ m}\cdot\text{s}^{-1}$) can reach the maximum of $276\text{ }\mu\text{m}$ at the position of the melt pool, with the resulting ultrasound intensity I_g being $35.5\text{ W}\cdot\text{cm}^{-2}$. The corresponding maximum ultrasonic energy in the Inconel 718 melt pool (I_m) is measured as $17.5\text{ W}\cdot\text{cm}^{-2}$ (with an absorption rate of 49.3%), which is below the melt cavitation threshold. It can only induce acoustic streaming, i.e., without cavitation, which is defined as the low-intensity ultrasound (or non-cavitation ultrasound).

Table 1 summarizes the ultrasonic intensity provided by the two approaches. It is worth mentioning that unlike the contact-transmission mode illustrated in Fig. 1b or other literatures¹⁹, the ultrasonic intensity by our non-contact-transmission mode is stable in the melt pool once the position of the ultrasonic transducer is decided, regardless of the size and geometry of deposited layers during the process.

Laser melting and deposition

To investigate the effects of ultrasound on the laser melting and deposition process, the experimental system constructed by the State Key Laboratory of Solidification Processing, China, comprises an IPG-3000W laser deposition processing center (consisting of a YSL-3000 fiber laser source, powder feeder, and protective gas device) and a contact-transmission/non-contact-transmission ultrasonic auxiliary device. The laser source has a maximum power output of 3000 W within the wavelength range of 900 nm to 1200 nm. The process was performed inside an enclosed chamber with a continuous flow of argon carrier gas, that also provides the necessary shielding environment. A powder feed rate of $15\text{ g}\cdot\text{min}^{-1}$ was, respectively, supplied for Inconel 718 and stainless steel 316 L particles that vary in size from 40 to $150\text{ }\mu\text{m}$ in diameter. Table 2 summarizes the laser parameters employed for the experiments. These values were selected based on a series of prior experiments without ultrasound to optimize the processing parameters and obtain dense samples. The ultrasound employed has a frequency of 20 kHz. For the contact-transmission

mode ultrasonic system, the transducer was rigidly bolted to the cylindrical substrate. For the non-contact-transmission mode, the transducer was securely mounted on the robotic arm using an adjustable holder, ensuring it remains focused on the laser spot as the laser moves, where the distance between the transducer and the melt pool was maintained at a constant value of 20.6 mm (corresponding to the maximum periodicity distance of 20 kHz ultrasound in argon gas) with the input angle of 150° .

Monitoring, microstructure and tensile property

A high-speed camera SKF with a laser source (Fu Huang Agile Device, Hefei, China) was employed to monitor the dynamic evolution of the melt pool during the process at a frame rate of 10000 frames per second. The distance between the camera and the melt pool was approximately 300 mm, with an angle of inclination from the horizontal direction set at 60° for photographing purposes. By utilizing both the laser brightening device (with an emission wavelength of 808 nm) and wavelength filter (400–850 nm visible waveband), clear dynamic evolutions of the melt pool can be captured.

To investigate the relative density and size, morphology, and alignment of the pores in the deposited samples, X-ray computed tomography (CT) was performed using a ZEISS Xradia 520 Versa 3D X-ray microscope at a voltage of 140 kV and a current of 100 μA , with a pixel size of $1.3\text{ }\mu\text{m}$. These images were then processed using the back-projection algorithm provided by the commercial software VG Studio to generate two-dimensional tomograms. Finally, the tomograms were input into the software Avizo for three-dimensional visualization and quantitative analysis. The tomographic images were then denoised using a non-local mean filter, and interactive thresholding was used to accurately differentiate between metal and pores. Afterward, volumetric rendering was utilized to reconstruct the samples and pores, which were then quantitatively evaluated for number, size, spatial morphology, and distribution by labeling analysis.

Prior to microstructure characterization analysis, the specimens underwent a series of post-treatments, including wire electrical discharge machining (EDM), grinding, mechanical polishing, ultrasonic cleaning, and etching ($8\text{ ml HCl} + 20\text{ ml C}_2\text{H}_6\text{OH} + 14\text{ g FeCl}_3$) to obtain a metallographic cross-section. The dendrite morphology was observed using an OM light microscope (VHX-2000, Keyence, Japan). In addition, the electron backscatter diffraction (EBSD) analysis was conducted using an SEM (Tescan, Mira3, accelerating voltage of 25 kV, probe current of 18 nA) equipped with an Oxford EBSD detector, and the step size is $5\text{ }\mu\text{m}$. The texture data and orientation information were obtained by the HKL-Channel 5 software. The grain size was counted using the equivalent circle diameter method.

In order to characterize the tensile properties, dog-bone-shaped rectangular specimens with a gauge cross-section of $9\text{ mm} \times 2\text{ mm}$ and a gauge length of 24 mm were fabricated from the printed specimens using EDM. To reduce the influence of the edge effect of the specimen on the experimental results, we select the middle region of the deposited block sample to prepare the tensile specimen, as shown in Supplementary Fig. 1. Before the tensile testing, the surfaces of the flat specimens were ground using 1500-grit SiC paper. A strain-gauged extensometer was utilized to measure the engineering strain within the gauge section. Tensile tests were performed at room temperature with a universal testing machine (manufactured by Sinotest Equipment Co.,

Table 1 | Ultrasonic intensity

	Low-intensity ultrasound by non-contact-transmission mode		High-intensity ultrasound by contact-transmission mode	
	$A_m, \mu\text{m}$	$I_m, \text{W}\cdot\text{cm}^{-2}$	$A_m, \mu\text{m}$	$I_m, \text{W}\cdot\text{cm}^{-2}$
Minimum	0.01	2.4×10^{-3}	3	212.4
Maximum	0.86	17.5	15	5320.2

For Inconel 718 and stainless steel 316 L, the low-intensity ultrasound provided by the non-contact-transmission mode is below the melt cavitation threshold, while the high-intensity ultrasound provided by the contact-transmission mode is above the melt cavitation threshold.

Table 2 | Experiment parameters for laser melting and deposition

Laser power (W)	Scanning speed ($\text{mm}\cdot\text{s}^{-1}$)	Powder feeding rate ($\text{g}\cdot\text{min}^{-1}$)	Gas flow rate ($\text{L}\cdot\text{min}^{-1}$)	Spot diameter (mm)
700	5	15	3.6	2

Ltd., DNS 10) at an engineering strain rate of $1\text{ mm}\cdot\text{min}^{-1}$. Tensile properties, including the yield strength, ultimate tensile strength, and elongation to fracture, were determined from the tensile engineering stress-strain curves.

High-fidelity simulation

The melt pool flow is simulated using a high-fidelity multi-physics model, customized on the commercial software FLOW-3D. For the contact ultrasound-aided AM case, the high-intensity ultrasound effect has been validated in our previous study²⁰. For the non-contact ultrasound-aided AM case, we simplify the ultrasound into multiple parallel ultrasonic rays and use the ray tracing method to trace the local interaction between the ultrasound and the melt pool surface. Because of the dynamic surface evolution, the instantaneous ultrasound propagation distance in the gas medium is tracked and incorporated in the model. The relationship between the ultrasound amplitude and propagation distance is derived based on experimental measurements. Specifically, in the case with maximum non-contact ultrasound intensity in the gas medium, the relationship is given as:

$$A_g = 104 + 366e^{\left(\frac{-x_g}{31}\right)} \quad (3)$$

where A_g denotes the ultrasound amplitude in the gas medium (μm), and x_g represents the ultrasound propagation distance (mm). At this time, the corresponding ultrasound intensity in the gas medium is given as:

$$I_g = 0.5\rho_g c_g (2\pi f A_g)^2 \quad (4)$$

where ρ_g and c_g are the gas medium density and sound speed in the gas medium. Considering the significant discrepancy in density between gas and melt pool, the absorbed ultrasonic intensity is calculated in Eq. (5):

$$I_m = \alpha I_g \quad (5)$$

where I_m denotes the ultrasonic intensity of melt pool and α represents the absorption of ultrasonic intensity. This absorption can be evaluated through experimental measurements. (Supplementary Fig. 2 and 3). Therefore, the ultrasound amplitude in the melt pool is given as:

$$A_m = \frac{\left(\frac{2I_m}{\rho_m c_m}\right)^{0.5}}{2\pi f} \quad (6)$$

where A_m , ρ_m and c_m are the ultrasound amplitude, fluid density and sound speed in the melt pool. Then, the differences of ultrasound propagation distance can also result in the phase discrepancy, given as:

$$\Phi = \frac{2\pi f x_g}{c_g} \quad (7)$$

where Φ is the local phase of the ultrasound. Consequently, the local force F_{ultra} caused by the ultrasound ray is given as:

$$F_{\text{ultra}} = -4\pi^2 V_m \rho_m f^2 A_m \sin(2\pi f t + \Phi) \quad (8)$$

where V_m denotes the melt volume. Further description of the model, detailed in our previous studies²⁰ will not be repeated. Parameters used in the model are listed in Supplementary Table 1. Moreover, quantitative comparison of the flow velocity at the melt pool surface between the numerical simulation and experimental test is conducted to validate the reliability of the numerical model (see the Supplementary information-F. Model Validation).

Reporting summary

Further information on research design is available in the Nature Portfolio Reporting Summary linked to this article.

Data availability

Source data are provided with this paper with raw movies available as supplementary data files. Any additional data is available upon request via the corresponding author. Source data are provided in this paper.

Code availability

The FLOW-3D software routine and custom code are not publicly available. All data generated using this code are available from the corresponding author.

References

- Pham, M.-S., Liu, C., Todd, I. & Lertthanasarn, J. Damage-tolerant architected materials inspired by crystal microstructure. *Nature* **565**, 305–311 (2019).
- Tan, C. et al. Additive manufacturing of bio-inspired multi-scale hierarchically strengthened lattice structures. *Int. J. Mach. Tools Manuf.* **167**, 103764 (2021).
- Feng, Z. et al. Influence of scale effect on surface morphology in laser powder bed fusion technology. *Virtual Phys. Prototyp.* **19**, e2336157 (2024).
- Qu, Z. et al. High fatigue resistance in a titanium alloy via near-void-free 3D printing. *Nature* **626**, 999–1004 (2024).
- Chen, H., Zhu, W., Tang, H. & Yan, W. Oriented structure of short fiber reinforced polymer composites processed by selective laser sintering: The role of powder-spreading process. *Int. J. Mach. Tools and Manuf.* **163**, 103703 (2021).
- Chen, H. & Yan, W. Spattering and denudation in laser powder bed fusion process: Multiphase flow modelling. *Acta Mater.* **196**, 154–167 (2020).
- Chen, H., Cheng, T., Wei, Q. & Yan, W. Dynamics of short fiber/polymer composite particles in paving process of additive manufacturing. *Addit. Manuf.* **47**, 102246 (2021).
- Chen, H., Cheng, T., Li, Z., Wei, Q. & Yan, W. Is high-speed powder spreading really unfavourable for the part quality of laser powder bed fusion additive manufacturing? *Acta Mater.* **231**, 117901 (2022).
- Chen, H. et al. Packing quality of powder layer during counter-rolling-type powder spreading process in additive manufacturing. *Int. J. Mach. Tools Manuf.* **153**, 103553 (2020).
- Sui, S. et al. The influence of Laves phases on the room temperature tensile properties of Inconel 718 fabricated by powder feeding laser additive manufacturing. *Acta Mater.* **164**, 413–427 (2019).
- Martin, J. H. et al. 3D printing of high-strength aluminium alloys. *Nature* **549**, 365–369 (2017).
- Chen, H. et al. Powder-spreading mechanisms in powder-bed-based additive manufacturing: Experiments and computational modeling. *Acta Mater.* **179**, 158–171 (2019).
- Tian, X. J., Zhang, S. Q., Li, A. & Wang, H. M. Effect of annealing temperature on the notch impact toughness of a laser melting deposited titanium alloy Ti-4Al-1.5Mn. *Mater. Sci. Eng. A* **527**, 1821–1827 (2010).
- Carroll, B. E., Palmer, T. A. & Beese, A. M. Anisotropic tensile behavior of Ti-6Al-4V components fabricated with directed energy deposition additive manufacturing. *Acta Mater.* **87**, 309–320 (2015).
- DebRoy, T. et al. Additive manufacturing of metallic components – Process, structure and properties. *Prog. Mater. Sci.* **92**, 112–224 (2018).
- Ren, Y. M. et al. Low cycle fatigue properties of Ti-6Al-4V alloy fabricated by high-power laser directed energy deposition: Experimental and prediction. *Int. J. Fatigue* **127**, 58–73 (2019).

17. Marmottant, P. & Hilgenfeldt, S. Controlled vesicle deformation and lysis by single oscillating bubbles. *Nature* **423**, 153–156 (2003).
18. Jung, J.-G. et al. Mechanism of ultrasound-induced microstructure modification in Al–Zr alloys. *Acta Mater.* **199**, 73–84 (2020).
19. Todaro, C. J. et al. Grain structure control during metal 3D printing by high-intensity ultrasound. *Nat. Commun.* **11**, 142 (2020).
20. Yang, Z. et al. Manipulating molten pool dynamics during metal 3D printing by ultrasound. *Appl. Phys. Rev.* **9**, 021416 (2022).
21. Todaro, C. J. et al. Grain refinement of stainless steel in ultrasound-assisted additive manufacturing. *Addit. Manuf.* **37**, 101632 (2021).
22. Wang, S. et al. In situ high speed imaging study and modelling of the fatigue fragmentation of dendritic structures in ultrasonic fields. *Acta Mater.* **165**, 388–397 (2019).
23. Wang, B. et al. Ultrafast synchrotron X-ray imaging studies of microstructure fragmentation in solidification under ultrasound. *Acta Mater.* **144**, 505–515 (2018).
24. Wang, F. et al. A synchrotron X-radiography study of the fragmentation and refinement of primary intermetallic particles in an Al-35 Cu alloy induced by ultrasonic melt processing. *Acta Mater.* **141**, 142–153 (2017).
25. Yuan, D., Shao, S., Guo, C., Jiang, F. & Wang, J. Grain refining of Ti-6Al-4V alloy fabricated by laser and wire additive manufacturing assisted with ultrasonic vibration. *Ultrason. Sonochem.* **73**, 105472 (2021).
26. Feng, X., Zhao, F., Jia, H., Li, Y. & Yang, Y. Numerical simulation of non-dendritic structure formation in Mg-Al alloy solidified with ultrasonic field. *Ultrason. Sonochem.* **40**, 113–119 (2018).
27. Yuan, T., Kou, S. & Luo, Z. Grain refining by ultrasonic stirring of the weld pool. *Acta Mater.* **106**, 144–154 (2016).
28. Puga, H., Barbosa, J., Machado, J. M. & Vilarinho, C. Ultrasonic grain refinement of die cast copper alloys. *J. Mater. Process. Technol.* **263**, 336–342 (2019).
29. Wu, D., Song, C., Di, T., Niu, F. & Ma, G. Intermetallic regulation mechanism of inconel 718/Ti6Al4V composite by novel follow-up ultrasonic assisted laser additive manufacturing. *Compos. Part B Eng.* **235**, 109736 (2022).
30. Lu, H. et al. Ultrasonic machining response and improvement mechanism for differentiated bio-CoCrMo alloys manufactured by directed energy deposition. *J. Mater. Sci. Technol.* **193**, 226–243 (2024).
31. Yadav, R., Das, Chakladar, N. & Paul, S. Tailoring of residual stress by ultrasonic vibration-assisted abrasive peening in liquid cavitation of metallic alloys. *Int. J. Mach. Tools Manuf.* **194**, 104100 (2024).
32. Ji, F. et al. Grain refinement and mechanism of steel in ultrasound assisted wire and arc additive manufacturing. *Int. Commun. Heat Mass Trans.* **143**, 106724 (2023).
33. Gorunov, A. I. Additive manufacturing of Ti6Al4V parts using ultrasonic assisted direct energy deposition. *J. Manuf. Process.* **59**, 545–556 (2020).
34. Yang, Z. et al. In-situ monitoring of the melt pool dynamics in ultrasound-assisted metal 3D printing using machine learning. *Virtual Phys. Prototyp.* **18**, e2251453 (2023).
35. Yang, Z. et al. Effects of ultrasound on multilayer forming mechanism of Inconel 718 in directed energy deposition. *Addit. Manuf.* **48**, 102462 (2021).
36. Ramirez, A., Qian, M., Davis, B., Wilks, T. & StJohn, D. H. Potency of high-intensity ultrasonic treatment for grain refinement of magnesium alloys. *Scr. Mater.* **59**, 19–22 (2008).
37. Bayat, M. et al. On the role of the powder stream on the heat and fluid flow conditions during Directed Energy Deposition of maraging steel-Multiphysics modeling and experimental validation. *Addit. Manuf.* **43**, 102021 (2021).
38. Hunt, J. D. Steady state columnar and equiaxed growth of dendrites and eutectic. *Mater. Sci. Eng.* **65**, 75–83 (1984).
39. Knapp, G. L., Raghavan, N., Plotkowski, A. & DebRoy, T. Experiments and simulations on solidification microstructure for Inconel 718 in powder bed fusion electron beam additive manufacturing. *Addit. Manuf.* **25**, 511–521 (2019).
40. Raghavan, N. et al. Numerical modeling of heat-transfer and the influence of process parameters on tailoring the grain morphology of IN718 in electron beam additive manufacturing. *Acta Mater.* **112**, 303–314 (2016).
41. Pilling, J. & Hellawell, A. Mechanical deformation of dendrites by fluid flow. *Metall. Mater. Trans. A* **27**, 229–232 (1996).
42. Zhang, T. & Yuan, H. Multiscale plasticity behavior and fatigue performance of laser melting multi-layer nickel-based superalloys upon heat treatments. *Int. J. Plast.* **158**, 103404 (2022).
43. Blairs, S. Correlation between surface tension, density, and sound velocity of liquid metals. *J. Colloid Interface Sci.* **302**, 312–314 (2006).

Acknowledgements

H.C., X.L., J.S.H., Y.J.S., Y.X.A., W.M.N. and H.O.Y. acknowledge National Key Research and Development Program of China (Grant No. 2023YFB4604703), National Natural Science Foundation of China (Grant No. U22A20189) and National Natural Science Foundation of China (Grant No. 52375382). S.H.W. acknowledges the support by the Post-doctoral Fellowship Program of CPSF (Grant No. GZC20232004). W.J.G. and W.T.Y. acknowledge the Ministry of Education, Singapore, under its Academic Research Fund Tier 2 (Grant No. MOE-T2EP50221-0013). W.H.Y. acknowledges the China Scholarship Council (Grant No. 202006160011). S.Y. and S.Y.R. acknowledge the European Innovation Council Pathfinder project (Grant No. 101046835).

Author contributions

J.S.H. conducted experiments, data curation and writing – original draft. S.H.W. conducted software, data curation and writing – original draft. W.J.G. conducted data curation and writing – original draft. H.C. conducted conceptualization, writing – original draft and reviewing, funding acquisition and supervision. Y.J.S. conducted the investigation and data curation. Y.X.A. conducted experiments. W.H.Y. conducted software and formal analysis. S.Y.R. conducted software and formal analysis. W.M.N. conducted experiments. H.O.Y. conducted an investigation and experiments. S.Y. conducted formal analysis. W.T.Y. conducted supervision, writing, reviewing and editing. X.L. conducted the review and supervision.

Competing interests

The authors declare no competing interests.

Additional information

Supplementary information The online version contains supplementary material available at <https://doi.org/10.1038/s41467-025-62803-w>.

Correspondence and requests for materials should be addressed to Hui Chen or Xin Lin.

Peer review information *Nature Communications* thanks Yuze Huang, Tongmin Wang, and the other anonymous reviewer(s) for their contribution to the peer review of this work. A peer review file is available.

Reprints and permissions information is available at <http://www.nature.com/reprints>

Publisher's note Springer Nature remains neutral with regard to jurisdictional claims in published maps and institutional affiliations.

Open Access This article is licensed under a Creative Commons Attribution-NonCommercial-NoDerivatives 4.0 International License, which permits any non-commercial use, sharing, distribution and reproduction in any medium or format, as long as you give appropriate credit to the original author(s) and the source, provide a link to the Creative Commons licence, and indicate if you modified the licensed material. You do not have permission under this licence to share adapted material derived from this article or parts of it. The images or other third party material in this article are included in the article's Creative Commons licence, unless indicated otherwise in a credit line to the material. If material is not included in the article's Creative Commons licence and your intended use is not permitted by statutory regulation or exceeds the permitted use, you will need to obtain permission directly from the copyright holder. To view a copy of this licence, visit <http://creativecommons.org/licenses/by-nc-nd/4.0/>.

© The Author(s) 2025